Acta Materialia 234 (2022) 117994

Contents lists available at ScienceDirect

Acta Materialia

journal homepage: www.elsevier.com/locate/actamat

Low power reconfigurable multilevel nanophotonic devices based on Sn-doped $Ge_2Sb_2Te_5$ thin films

Petr Lazarenko[a,*], Vadim Kovalyuk[b,i,j], Pavel An[b,j], Sergey Kozyukhin[c,d], Viktor Takáts[e], Alexander Golikov[a,b], Victoria Glukhenkaya[a], Yuri Vorobyov[f], Timur Kulevoy[g], Aleksey Prokhodtsov[h], Alexey Sherchenkov[a], Gregory Goltsman[b,h,b]

[a] National Research University of Electronic Technology, Zelenograd 124498, Russia
[b] Moscow State Pedagogical University, Moscow 119992, Russia
[c] Kurnakov Institute of General and Inorganic Chemistry of Russian Academy of Sciences, Moscow 119991, Russia
[d] National Research Tomsk State University, Tomsk 634050, Russia
[e] Institute for Nuclear Research, Hungarian Academy of Sciences, Debrecen 4026, Hungary
[f] Ryazan State Radio Engineering University, Ryazan 390005, Russia
[g] National Research Center "Kurchatov Institute"-ITEP, Moscow 117218, Russia
[h] National Research University Higher School of Economics, Moscow 101000, Russia
[i] NTI Center for Quantum Communications, National University of Science and Technology MISiS, Leninsky prospekt 4, Moscow 119049, Russia
[j] Russian Quantum Center, Skolkovo 143025, Moscow, Russia

ARTICLE INFO

Article history:
Received 30 November 2020
Revised 19 April 2022
Accepted 2 May 2022
Available online 3 May 2022

Keywords:
Phase change materials
Chalcogenide
$Ge_2Sb_2Te_5$
Doping
Integrated optics devices

ABSTRACT

In the past years, $Ge_2Sb_2Te_5$ has been considered a promising functional material for a variety of reconfigurable multilevel devices, including photonic integrated circuits for the post-von Neumann arithmetic processing. However, despite significant advances, it is necessary to reduce the switching energy of $Ge_2Sb_2Te_5$ for creation of the on-chip low power all-photonic spiking neural networks. The present work focuses on the effect of tin ion implantation on the properties of amorphous $Ge_2Sb_2Te_5$ thin films, as well as on the performance of Mach-Zehnder interferometers and balanced beam splitters based on them. As a result, Sn-doping accompanied by the formation of weaker bonds in $Ge_2Sb_2Te_5$ thin films is an efficient approach to significantly reduce the threshold energy of fs-laser initiated phase transitions and change the effective absorption coefficient. The possibility of using the Sn-doped $Ge_2Sb_2Te_5$ thin films for fully optical multilevel reversible recording between 9 different levels (3 bits) has been demonstrated by experimental measurements of fabricated on-chip balanced beam splitters. The obtained results show that the Sn doping of $Ge_2Sb_2Te_5$ layer can be used to optimize the properties of the GST225 thin films, in particular to reduce the switching energy. So, it has the potential to improve the characteristics of reconfigurable multilevel nanophotonic devices using the GST225 thin films, including fully non-volatile memory and developed on-chip low power all-photonic circuits for post-von Neumann arithmetic processing.

1. Introduction

Improvement of the methods of optical data transfer and processing have led to rapid development of photonic integrated circuits (PICs) [1,2]. Application of PICs should significantly improve the performance of modern devices. Creation of fully integrated PICs can be enhanced by different nonvolatile nanophotonic elements allowing to control parameters of optical signals (intensity, wavelength shifts, shape and position of the resonance wavelength, etc.). The usage of the telluride based phase change memory materials (PCMs) is one of the ways to create reconfigurable nanophotonic elements for PICs.

The chalcogenide $Ge_2Sb_2Te_5$ (GST225) is one of several functional materials which has already been in wide use for different purposes, in particular, for optical discs (DVD, Blu-Ray) [3] and electrical memory (PCRAM) [4] - in contrast to "promising" memory device materials that remain "promising" and nothing more for decades. Thin films of GST225 are actively used in commercially successful rewritable optical [3] and electrical [5] storage applications, as well as in reflective displays [6], active antennas in the middle IR range [7], thermal camouflage [8], hologram ele-

* Corresponding author.
E-mail addresses: lpi@org.miet.ru (P. Lazarenko), alexabrest@yandex.ru (A. Prokhodtsov).

https://doi.org/10.1016/j.actamat.2022.117994
1359-6454/

ments [9] currently being developed. The wide application of this compound is connected with the good combination of its physicochemical properties such as rapid phase transitions (less than 50 ns) [10], sufficient stability of the phase states [11], significant change in the optical and electrical properties of the chalcogenide semiconductor films during phase transformations [12]. Also, the large optical contrast between amorphous and crystalline phases of GST225 thin film makes it possible to create multilevel devices due to different crystallization degrees [13].

The unique characteristics of GST225 material can be attributed to a combination of different factors. The authors of several works [11,14–16] showed that the structural features of the amorphous and metastable (rocksalt) phases, in particular a large concentration of vacancies, are a significant factor in explaining the ultrafast phase transition between amorphous and metastable phases. At the same time, to elucidate the specific properties such as optical and electrical contrast between amorphous and crystalline states, it is necessary to consider the factors associated with the difference between the bonds and the atomic arrangement in both phases. Various mechanisms have been proposed to describe the formation and stabilization of the "long" and "short" Ge-Te chemical bonds (also called the metavalent bonds), such as the models based on the resonance bond [17–19] and Peierls distortion [19–21]. For instance, certain related materials were compared in the works [18,22]. There, the possibility of explaining the switching and significant contrast of the properties of GeTe, PbTe, GeS, Sb_2Te_3, Bi_2Se_3, $AgSbTe_2$ and GST225 between amorphous and crystalline states was demonstrated from the standpoint of the metavalent bonding mechanism.

Combination of the GST225 advantages with modern achievements in nanophotonics should allow to create a variety of reconfigurable multilevel devices, for example, multilevel on-chip nonvolatile memory [23,24] or post-von Neumann arithmetic processing [25]. The operating principle of those devices is based on the significant changes in the optical properties of GST225 thin cover during phase transitions between amorphous and crystalline states. As a result, crystallization and amorphization processes in GST225 are accompanied by changes of waveguide's optical losses. At present, the possibility of controlling the parameters of an optical signal in a linear waveguide structure [26], micro-ring resonator [27] and interferometers [28] by changing the phase state of the GST225 material have been demonstrated.

Significant progress was made in the fabrication of hybrid nanophotonic devices using the GST225 thin films, and their benefits were demonstrated on separate devices. However, the transition to large-scale PICs, including hundreds and thousands of components, requires a substantial reduction in the switching energy of the GST225 during the writing and erasing operations. The search for materials with lower switching energy than GST225 is especially important to create fast all-photonic spiking neural networks [29].

To improve the performance of phase-change memory devices (speed, power consumption, interlevel contrast, optical losses at operating wavelengths, etc.) several approaches are used:

1) the search for alternative GST225 compositions is in progress (Ag-In-Sb-Te, Se-Sb-Te, Sc-doped Sb_2Te_3 [30], Sb_2Se_3, Sb_2S_3 [31], etc.); 2) the variation of the element content within the Ge-Sb-Te system ($GeSb_4Te_7$, $GeSb_2Te_4$, GST225, $Ge_8Sb_2Te_{11}$, etc.); 3) attempts are being made to use the heterostructures formed by alternating GeTe and Sb_2Te_3 monolayers [32]; 4) various modifying impurities are introduced into GST225. It should be noted that each of the approaches can be an effective improvement tool for specific areas of application. For example, it was shown in [32] that replacing the GST225 with Sb_2Se_3 and Sb_2S_3 leads to a decrease in optical losses due to a decrease in the absorption of functional layers.

However, a radical change in the used material leads to a change in all the device parameters and switching strategies that have been worked out for the GST225. So, one of the main advantages of doping is the possibility to carry out the targeted precision tuning of the characteristics of the created structure based on the GST225 which has already approved itself as a brilliant material for phase-change memory devices and has been studied in sufficient detail.

Nevertheless, modification of the characteristics of chalcogenide vitreous semiconductors is a complex problem due to their low sensitivity to doping, and this distinguishes them from crystalline semiconductors such as Si or Ge. Currently, a large number of works have been published investigating the influence of the various dopants (N [33], O [34], C [35], Mg [36], Al [37], Si [38], *Sc* [30], Ti [39], V [40], Cr [41], Ni [42], Cu [43], Zn [44], As [45], Se [46], Mo [47], Ag [48], In [49], Sn [50], Sm [51], Bi [52], W [53], and et al.) on the properties of Ge-Sb-Te thin films. A number of the listed impurities, for example, carbon, tin, scandium and zinc, can help energy-saving and accurate multi-state formation. However, in the present study, we focused on the tin as a dopant element for GST225, used as a functional layer of the nanophotonic devices. Our motivation was as follows.

First, the Sn introduction into amorphous GST225 thin films leads to a decrease of the duration of laser pulse required to initiate the crystallization process, which was demonstrated by R. Kojima et al. [54] and confirmed by other studies [55]. According to the data of Raman spectroscopy [56] and X-ray diffraction [50] for GST225 thin films doped by Sn, it can be stated that the introduction of tin atoms leads to a noticeable change in the vibrational bonds and the parameters of the structure. The Sn and Ge are isovalent and isomorphic elements with close values of electronegativity. So, we can expect the replacement of the germanium (cation site) by tin and the formation of Sn-Te bonds without significant lattice disturbance. This replacement of Ge atoms by Sn will be accompanied by a sufficient decrease of the binding energies from 402 kJ/mol for the Ge–Te bond to 319.2 kJ/mol for that of Sn–Te [57]. In this case, even a small amount of Sn dopant can change the switching parameters for the GST225 thin film, in particular, reduce the energy needed to initiate the phase transitions. This assumption is indirectly confirmed by the change in crystallization behavior [58] and observed decrease in the temperature [59], threshold current [60] or laser radiation energy [61–63] required for crystallization. However, it has been argued in some works [64–66] that introduction of the tin dopant into the GST225 phase change material slightly increases the crystallization temperature.

Second, analysis of the results [33–53] shows that for the sufficient variation of properties, dopant atoms must have close parameters to those of the components of GST225, providing incorporation of the dopant atoms into the lattice with minimal stresses. Otherwise, phase separation and element segregation may occur during both the writing and erasing processes in devices based on the PCMs. According to the results of the calculation of the doping formation energy obtained through the computational dopant screening process [67], tin has the greatest thermodynamic stability of the substitutional dopant in GST225, compared with the most elements used for doping Ge-Sb-Te. Moreover, despite the increase of the lattice parameters for the crystalline states [55] due to a noticeable difference in the covalent radii of Sn (1.44 Å) and Ge (1.22 Å), an introduction of low Sn concentrations should not significantly affect the material stability. The results of the study [68] confirm that a phase separation on GST225 and SnTe during the crystallization process is observed only in case of large Sn concentrations above 11.6 at.%. The phase separation can lead to an increase in the crystallization temperature [69]. However, even in case of a two-phase separation, GST225 (fcc) and SnTe (cubic lat-

tice) have a similar structure, so the doping should not significantly influence the phase stability of devices based on the PCMs [68]. In this study, we use a low Sn concentration (less than 2 at.%) to minimize the probability of the phase separation. Herewith, another distinctive feature of this work is the application of the ion implantation method as a way to provide a chemical modification. This method is widely used in the microelectronic industry, and its potential for modifying layers of the phase change memory materials has been noted in [35,70,71]. The attractiveness of this method lies in the possibility of creating the necessary concentration profiles of impurities in thin films in a wide range of temperatures, including low temperatures, which is extremely important for doping thin films of amorphous materials.

Third, optimal operation of nanophotonic devices requires a well-suited combination of optical properties for PCMs. Most studies [59-63,68] focus on the influence of Sn dopant on the optical reflection contrast that was detected by spectrophotometry and ellipsometry from large areas of thin films. For the first time, we determined the effect of the tin dopant on the absorption coefficient of the amorphous and crystalline GST225 cover using the results of a direct study of fabricated waveguide structures. These results will help to predict the influence of tin dopant on the operation of integrated nanophotonic devices at a telecommunication wavelength of 1550 nm more accurately, as well as to optimize of their construction.

Thus, the aim of this study is to investigate the effect of tin ion implantation on the structural, optical and laser switching properties of GST225 thin films, as well as on the properties of hybrid multilevel nanophotonic components on their basis.

2. Methods

2.1. Fabrication of on-chip silicon nitride nanophotonic devices

On-chip nanophotonic devices, including Mach-Zehnder interferometers, balance splitters, as well as freely lying GST225 cells, were fabricated on the basis of multilayer dielectric structures. Silicon was used as a substrate, covered by wet thermal silicon dioxide (2.6 μm) and then by stoichiometric low pressure chemical vapor deposited (LPCVD) silicon nitride with a thickness of 450 nm. The fabrication process included six main steps **(Supplementary Information, Fig. S1).**

During the first stage, using the photolithography, Ti/Au thermal evaporation and lift-off process, the alignment marks were formed. In the second stage, using electron-beam (e-beam) lithography, an image of the Si_3N_4 waveguides in the positive resist ZEP 520A was written. After development in O-Xylene, the stage was completed by reactive ion etching (RIE) in CHF_3 atmosphere. In the third stage, the next e-beam lithography process which determined the location and size of the GST225 cells atop of Mach-Zehnder interferometers (MZIs) and balanced splitters (BSs) was performed. In the fourth stage, the initial amorphous GST225 films with a thickness of about 30 nm were deposited at room temperature by DC magnetron sputtering of the polycrystalline target. Two identical sets of nanophotonic circuits on the same chip with the same parameters were prepared.

In the fifth stage, the ion implantation method was used to introduce Sn impurity into GST225 layers. Ion implantation is a doping method which is very often used in microelectronics to change the thin films properties. Accelerated ions can penetrate from nanometers to micrometers deep into the material, depending on the ion energy and chemical composition of the material. By choosing appropriate implantation parameters and film thickness, uniform Sn distribution along the film depth and homogeneous properties can be provided. Additionally, by varying the dose, thin film samples with different impurity concentrations can be obtained. So, tin ion implantation can be used to optimize the properties of amorphous GST225 thin films. The ion implantation into the GST225 was carried out by Multipurpose Test Bench (MTB). The MTB consists of the MEVVA type ion source, an electrostatic focusing system, a system of current and a beam profile measurements. The charge state distribution of the tin beam generated by MEVVA was measured by the time-of-flight method. Except for the initial 15 μs, the distribution was stable, and the beam consists of 43% of Sn^{1+} ions and 57% of Sn^{2+} ions. The beam irregularity at the target position was ±10%. The Sn ion implantation was carried out at 41±1 kV accelerating voltage with the beam pulse length of 250 μs and the repetition rate of 2 pps. A more detailed description of the implantation process is presented in [72]. A series of samples with a different concentration of an Sn dopant was prepared. We used $2.8 \cdot 10^{14}$, $1.4 \cdot 10^{14}$, $0.7 \cdot 10^{14}$ and $0.14 \cdot 10^{14}$ p/cm^2 fluences for the Sn implantation, which were calculated for the Sn concentrations in GST225 film of 2.0, 1.0, 0.5 and 0.1 at.%, respectively. The half of the devices was covered by a bulk rigid metal mask for protection, the other half was opened during the Sn implantation process.

In the sixth step, a silica coating layer was used to prevent oxidation during the investigation. The lift-off in acetone completed the procedure of nanophotonic devices fabrication. The micrograph of one of the fabricated devices is shown in Fig. 1.

2.2. Measurement setups

The uniformities of element distributions across the thickness of the investigated thin films were determined by Auger electron (AES, Physical Electronics PHI-670xi) and Time-of-Flight Secondary Ion Mass (TOF-SIMS, Ion TOF ToF.SIMS 5) spectrometries. Depth profiles of atomic concentrations of elements were obtained by the AES method using sample sputtering by an Ar^+ ion beam (2 kV, 0.35 μA). In the interval between the etching steps, the surface of samples was analyzed by an electron beam (5 kV, 20 nA). The diameter of the analyzed area was 100 μm. Concentrations of elements were determined in accordance with the model of homogeneous distribution of components using element sensitivity coefficients method. The Sn profiles were obtained only for the thin films after implantation with fluences above $2.8 \cdot 10^{14}$ p/cm^2, which is connected with the resolution of the used AES spectrometer. The TOF-SIMS analyses were performed using a Bi^+ analysis beam (30 kV, 15 pA) and a Cs^+ sputtering beam. Accelerating voltage for the etching was chosen to be 500 V for optimal depth resolution, as in this etching regime additional relief does not appear on the sample. The sputtering raster area was 300 ×300 μm^2 and the analysis area was 100 × 100 μm^2.

The structure changes were investigated by the Raman study, we used HORIBA LabRAM HR Evolution spectrometer with 514 nm excitation wavelength, 600 lines/mm diffraction grating, Olympus MPlan N 100 × 0.9 NA objective (built-in microscope Olympus BX41), and a laser spot of 4 μm in diameter. The excitation power was limited to 0.1 mW to avoid heating effect during the acquisition of spectra. A standard Horiba Raman edge filter was used (XR3001, 520AELP). The cut off of the filter was 50 cm^{-1}. A CCD matrix detector was used for spectra recording. The accumulation time and accumulation number were 20 s and 4, respectively. The calibration of the LabRAM HR spectrometer was verified before and after each investigated sample by acquiring Raman spectra of a standard silicon wafer.

The chemical states of the investigated thin films were investigated by X-ray Photoelectron Spectroscopy (XPS). We used the XPS equipped by an Al/Mg twin anode non-monochromatized X-ray source and Phoibos 100 MCD-5 series hemispherical energy analyzer produced by Specs GmbH. The samples were preliminarily etched by Argon-ion plasma in order to clean the surface as the

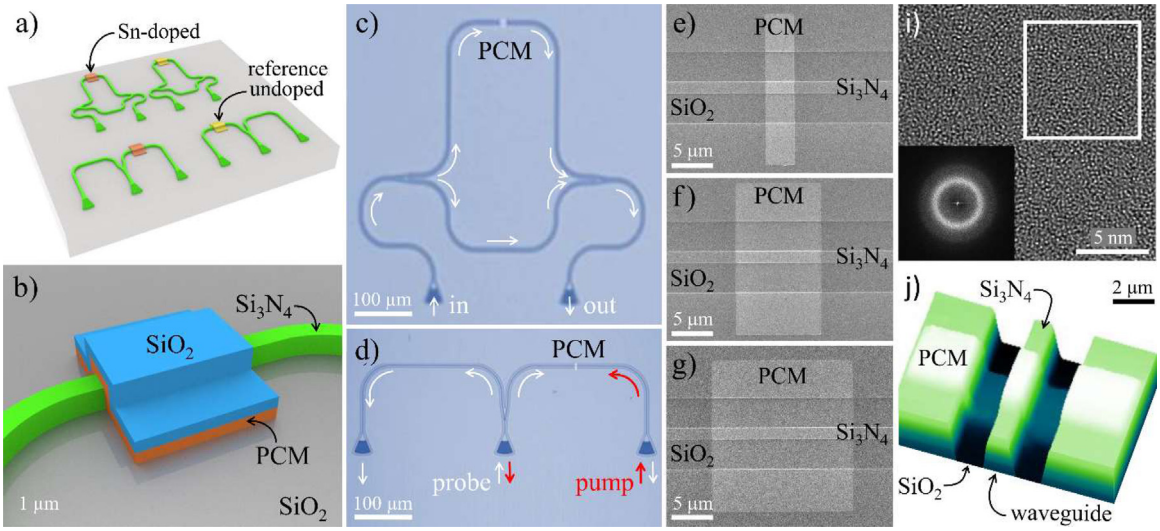

Fig. 1. The fabricated nanophotonic devices and the results of their analysis. (a) The schematic view of two types of on-chip nanophotonic devices: Mach-Zehnder interferometers and balanced splitters with Sn-doped GST225 (left) and undoped GST225 (right). (b) The schematic of PCM cell. (c, d) Optical micrographs of the fabricated MZI and BS with PCM cell on one of the arms. The white and red arrows show the directions of light propagation for the probe and pump laser signals, respectively. (e-g) Scanning electron microscopy images of PCM cells with different lengths (4, 12, 20 μm) on top of a rib silicon nitride waveguide. (i) TEM image and Fourier transform pattern (insets) for amorphous GST225 thin film. (j) Morphology of the one of the fabricated PCM cells obtained by means of an atomic force microscope.

samples were exposed to air. During the measurements, the samples were cooled down to the liquid Nitrogen temperature to avoid any heating originating from the X-ray source exposure. In order to determine the chemical environment of the Ge–Sb–Te system, the XPS spectra acquired were decomposed by the CasaXPS program.

A spectroscopic ellipsometer (Horiba Uvisel 2) was used to measure the optical constants in the range from 190 to 2100 nm with wavelength steps of 5 nm. To extract the refractive index and the extinction coefficient of GST225 thin films, the ellipsometric spectra were evaluated by a PsiDelta program using a five-layer model (air - surface - GST225 - SiO_2 - Si). The surface roughness was defined by effective medium approximation (a mixture of 50% film and 50% void). A single Tauc-Lorentz (TL) oscillator was applied to calculate the refractive index (n) and the extinction coefficient (k) spectra of the amorphous Sn-doped GST225 films.

The undoped and implanted samples were irradiated by the Yb:KGW femtosecond laser Pharos SP (Light Conversion) with the wavelength of 1030 nm. The pulse duration and the repetition rate were 180 fs and 200 kHz, respectively. The Gaussian beam profile was recorded using a CCD camera Spiricon SP620U (Ophir). The diameter of the normally incident laser beam at the sample plane was about 65 μm ($1/e^2$). During the light exposure the films were moved in the plane perpendicular to the light beam by the Aerotech ABL1000 air-bearing high precision 3D translation stage. We used the sets of 500 pulses and the repetition rate of 200 kHz for the laser irradiation of the investigated thin film samples. Schematic view of the experimental setup is shown in Supplementary information, Fig. S2. Microscopy of the modified areas was performed using an optical microscope with a 100 × 0.9 NA objective lens (Carl Zeiss Axiovert 40 MAC).

We used a setup that includes a precisely movable *x, y, z*, angle stage with picomotors (New Focus 8303), a tunable laser source (New Focus TLB 6600) and an optical microscope for preliminary alignment. Light entered the fiber array through a polarization controller with a period of 250 μm, located at an angle of 8° to the chip normal. After passing through nanophotonic devices, the transmission spectrum was measured by a fast photodetector (Hamamatsu G9801), the electrical signal from which was amplified and recorded by a data acquisition system.

The experimental setup for the multilevel reversible recording was realized using a pump-probe scheme. The pump pulses were formed using a laser (TeraXion - PureSpectrum NLL) in a standby mode. We used a programmable RF generator (Highlandtechnology - P400) as a trigger source. The RF pulse of the generator initiated the generation of laser radiation, wherein the profile of the electric and optical pulses was similar in shape. Further, the pump pulse was amplified (Keopsys CEFA-C-PB-HP) and then passed through a programmable attenuator (EXFO - FVA-600) which made it possible to control the amplitude (power) of the optical pulse. To read the transmission changes in the PCMs, we used CW probe light from the second laser (NewFocus TLB-6600). Optical circulators were used to ensure the independence of the pump and probe channels (Supplementary Information, Fig. S3).

3. Results and discussions

3.1. Fabrication of on-chip silicon nitride nanophotonic devices

We fabricated samples with double sets of two types of nanophotonic devices based on the silicon nitride waveguides (Fig. 1a, b). The first type of devices is MZIs, which were used to investigate the amorpous and crystalline thin films as a part of waveguide devices (Fig. 1c). The second type is BSs, which were used to demonstrate a multilevel reversible switching of the samples with Sn-doped GST225 by pump and probe laser pulses (Fig. 1d). A detailed description of the fabrication process and measurement setups is presented in the experimental section, here we only focus on the main features of the fabricated samples.

The thin coverings of GST225 were formed on one of the arms of devices. Each set of the samples includes devices with different lengths of GST225 thin coatings along the waveguide, which varied from 4 to 20 μm (Fig. 1e-g). We fabricated four samples with different Sn-concentrations (0.1, 0.5, 1.0, 2.0 at.%). It should be noted that each sample had the sets with the Sn-doped GST225 and the reference undoped GST225 (Fig. 1a), which was protected by a rigid metal mask during the Sn implantation process (Supplementary Information, Fig. S1). The results of transmission electron microscopy (TEM) and of the Fourier transform pattern analysis (Fig. 1i) determined the amorphous state for obtained thin films.

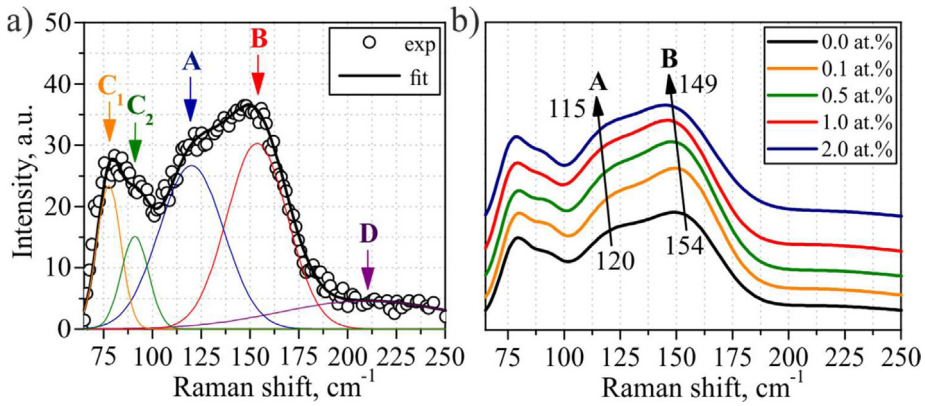

Fig. 2. The experimental Raman scattering spectrum of the amorphous GST225 film compared with the fitting results (a) and spectra of the thin films with a different amount of Sn dopant (b).

The composition measurements along the thickness of the fabricated thin films are shown in Supplementary Information, Fig. S4. The composition of the films is close to $Ge_2Sb_2Te_5$ and has uniform elemental distribution along the film thickness. It should be noted, that investigated samples have very thin (4–5 nm) amorphous oxide layer at the film surface, the residual amount of oxygen is less than 3 at.% and the same for all the investigated films.

In order to avoid the influence of the atmosphere [73] on the PCM thin films during the switching process, the fabricated films were coated with SiO_2 thin films (Fig. 1b). In most works [23,26,74-76] an ITO cap layer was used. Our choice of SiO_2 instead of ITO is based on its higher transparency in wavelength range near 1550 nm, which makes it possible to minimize optical losses of the additional energy on the absorption by this layer. The AFM-scan of one of the PCM areas of the sample after all technological operations is shown in Fig. 1(j).

Thus, two types of devices with different lengths of the PCM coverings based on Sn-doped and reference undoped GST225 were available. This provided us with an opportunity to compare their characteristics.

3.2. Investigation of as-deposited Sn-doped GST225 thin films

As it was noted in the introduction, effective property control of the GST225 thin films is possible if the impurities in the structure of the material are incorporated. In the present work, we used Raman spectroscopy and XPS to determine the influence of implanted tin ions on the peculiarities of structure modification in GST225 thin films.

Raman spectroscopy was used to determine the impact of the tin dopant (0.1, 0.5, 1.0, and 2.0 at.% Sn) on the structure peculiarities of amorphous GST225 thin films. The experimental Raman spectrum of the as-deposited undoped GST225 thin film measured in the frequency range from 65 to 250 cm^{-1} is shown in Fig. 2(a). The deconvolution of initial Raman spectrum was carried out using Gaussian fitting. Also, the positions and values of full width at half maximum (FWHM) for the deconvoluted peaks are presented in Table 1.

In the broadband frequency range 100–180 cm^{-1} two characteristic overlapping peaks A and B can be observed. The appearance of the intense peak A at $\sim$ 120 cm^{-1} can be attributed to the A_1 mode vibrations of the $GeTe_{4-n}Ge_n$ (n = 2, 3) corner-sharing tetrahedra, which was mentioned in several works [77–80].

The origin of the peak B ($\sim$ 154 cm^{-1}) can be explained using two different approaches. In [81,82] the appearance of the peak B is attributed to the vibrations of corner-edge $GeTe_{4-n}Ge_n$ tetrahedra (n = 2, 3). On the other hand, the stoichiometry composition of the studied material corresponds to the quasi-binary GeTe - Sb_2Te_3 alloy, and it seems possible to distinguish the contributions of both components to the experimentally observed spectra. So, a more convincing version which most researchers support is that this peak is caused by Sb–Te vibrations (stretching $A^2{}_{1g}$-modes) in $SbTe_3$ pyramidal units [79,82-85] or is connected to the defective octahedral coordination of Sb atoms [77,78,80,86].

The peaks C_1 at 78 cm^{-1} and C_2 at 91 cm^{-1} may correspond to the E-mode vibrations of the threefold coordinated Te atoms and Ge atoms located in $GeTe_4$ tetrahedral sites [80,81,83,85,87]. It should be noted that the boson peak tail (region of 30–45 cm^{-1}) [88] and used edge filter (cut off is 50 cm^{-1}) could influence the shape of the spectra at the low frequency range. The broad and high-frequency peak D ($\sim$ 210 cm^{-1}) can be explained by the F_2-mode vibrations of a $GeTe_4$ tetrahedra [77,78,80,82,83]. However, the characterization of the amorphous GST225 by only the tetrahedral Ge atoms is questionable. An alternative approach currently being considered is that the amorphous GST225 is also mostly octahedral, yet with more pronounced Peierls distortions than the corresponding crystalline state [19,21].

The tin implantation leads to redshifts of the main peaks A and B. These changes in peak positions become more noticeable as the dopant concentration increases. (see Fig. 2b).

With the rising tin concentration up to 2.0 at.% the peak A position shifts to $\sim$ 115 cm^{-1}. This change is probably due to the formation of Sn–Te bonds during tin ions implantation and, as a result, structural units of $SnTe_{4-n}Sn_n$ (n = 2, 3) coexisting together with the $GeTe_{4-n}Ge_n$ (n = 2, 3) structural units. Formation of the new units occurs according to the mechanism of substitution and causes effective replacement of Ge atoms by Sn. Moreover, replacement of Ge atoms by Sn is accompanied by a decrease in binding energies from 420 kJ/mol for the Ge–Te bond to 319.2 kJ/mol for that of Sn–Te [59] Therefore, the formation of these new structural units is highly likely and can lead to a shift of the peak A position to lower wavenumbers.

The peak B position also shifts to the lower frequency range (from 154 cm^{-1} for undoped thin films to ~149 cm^{-1} for films with 2.0 at.% Sn). In this case, similar arguments in favor of Sb substitution by Sn with the formation of Sn_2Te_3 and Sn_3Te_2 in the SnTe sublattice seem to be doubtful. This substitution is not energetically favorable demanding more energy than it is required to create Sb-Te bond (277.4 kJ/mol) [57]. The changes in short-range order and redistribution of electron density in the local area caused by tin ion implantation are more plausible explanations of the peak B position shift. It is known that peak shifts in the Raman spectra are due to the appearance of stresses in the structure caused by a change in bond lengths [89].

Table 1
Positions and full width at half maximums of the deconvoluted peaks of Raman spectra.

Sn,at.%	C_1		C_2		A		B		D	
	peak position (cm^{-1})	FWHM (cm^{-1})	peak position (cm^{-1})	FWHM(cm^{-1})	peak position (cm^{-1})	FWHM(cm^{-1})	peak position (cm^{-1})	FWHM(cm^{-1})	peak position (cm^{-1})	FWHM(cm^{-1})
0.0	78	7.3	91	8.3	120	19.5	154	18.3	210	52.0
0.1	78	7.3	91	8.3	120	19.4	154	18.2	210	52.0
0.5	78	7.3	90	8.3	119	19.4	152	18.8	210	52.0
1.0	77	7.3	89	8.3	117	19.8	151	18.6	210	52.0
2.0	77	7.0	89	8.3	115	19.0	149	19.0	210	52.0

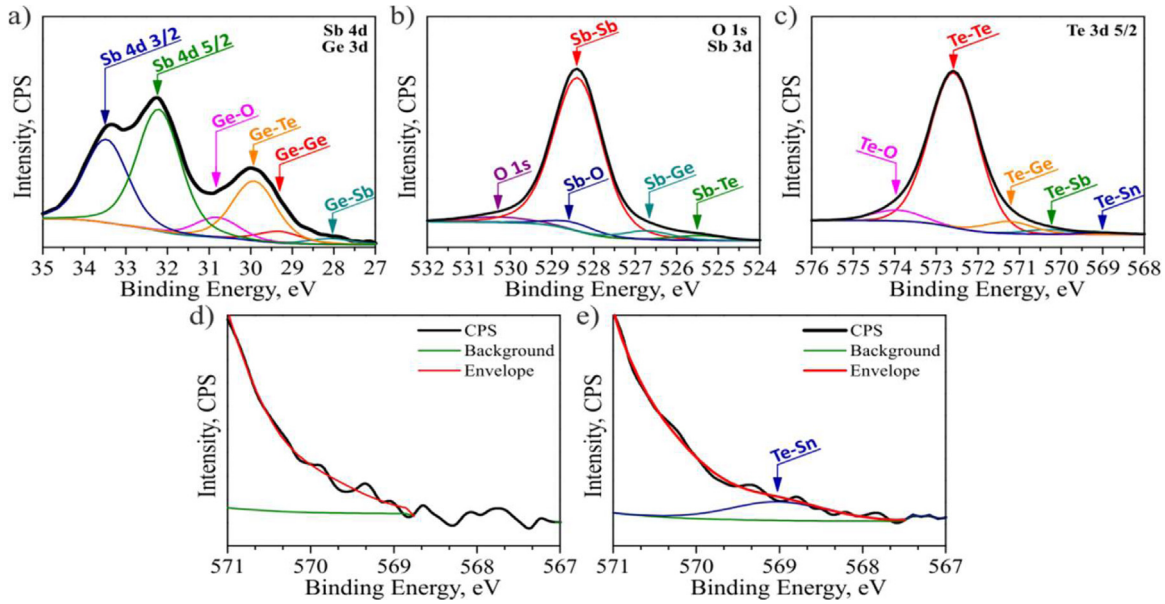

Fig. 3. Results of the XPS spectra peak decompositions for the GST225 thin film with 2 at.% of Sn for Ge 3d (a), Sb 3d (b), and Te 3d (c) electron core levels; and detailed Te 3d electron core level spectra for the undoped GST225 (d) and GST225 with 2 at.% of Sn (e).

Table 2
Results of XPS spectra decomposition for each chemical binding and different doping levels.

Sn,at.%	Te 3d 5/2				Ge 3d			Sb 3d
	Te-Te (%)	Te-Ge (%)	Te-Sb (%)	Te-Sn (%)	Ge-Te (%)	Ge-Ge (%)	Ge-Sb (%)	Sb-Sb (%)
0.0	93.6	6.0	1.4	0	70.9	23.7	5.4	94.1
0.5	92.1	6.3	1.5	0.1	70.7	23.6	5.7	91.4
1.0	91.4	6.4	1.6	0.6	76.5	16.5	7	91.1
2.0	89.5	6.9	2.6	1	77.6	14.9	7.4	91.9

In the amorphous state, the change in the length of Te–Sb bonds is associated with the change in the position of Ge atoms. According to [90], the lengths of long and short bonds of Ge–Te in the GST225 structure become longer and shorter with impurity introduction. This also can lead to lattice deformations and changes in the A^2_{1g} mode vibration frequency of the Sb_2Te_3 structural units.

The obtained XPS spectra of the components were measured and decomposed in order to investigate the bond breaking and bond switching mechanism induced by the variation in the amount of the Sn dopant. The results of peak decomposition are shown in Fig. 3 and spectra decomposition for each chemical binding and doping level are summarized in Table 2. A small amount of residual oxygen, which occurs in the spectra, is less than 3 at.% and is the same for all the investigated films. Due to the XPS sensitivity level, the samples with doping level below 0.5 at.% of Sn were not decomposed and are not included there.

The formation mechanism of the new chemical state caused by the doping is that the amount of the Te–Te homopolar bonds decreases as the Sn dopant concentration increases. As a result, new Te–Ge, Te–Sb and Te–Sn heteropolar bonds appear and increase. The same behavior is demonstrated by the Sb bondings. The amount of homopolar Sb-Sb bonds decreases, while new Te–Sb and Ge–Sb heteropolar bonds form and the doping level goes up.

It should be mentioned that introduction of Sn atoms is accompanied by the formation of new heteropolar bonds of Sn with Te only, which is explained by the higher binding energies of Te–Ge than that of Te–Sn. For the same reason we haven't seen any of Ge–Sn bonds.

So, analysis of Raman and XPS results for Sn-doped GST225 thin films showed that in the process of tin ion implantation Ge atoms are efficiently replaced by Sn owing to the formation of new low-energy heteropolar Sn–Te bonds. Formation of these bonds can lead to a decrease of the crystallization and amorphization energies.

The optical properties of the PCMs are crucial for the switching processes in the reconfigurable nanophotonic elements being developed, including energy consumption. Introduction of Sn dopant

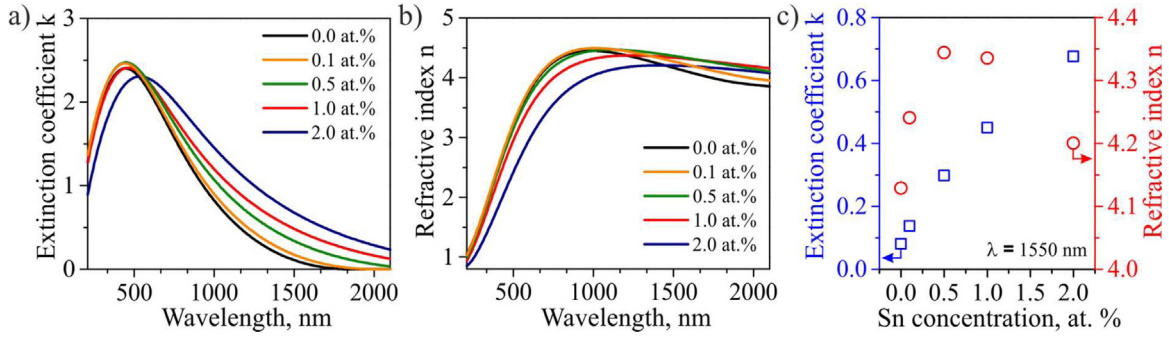

Fig. 4. Influence of Sn doping on the spectra of the extinction coefficient (a) and refractive index (b), and on the optical constants at 1550 nm (c).

into GST225 thin films, accompanied by the determined changes of the chemical bonds, should lead to changes in their spectra of extinction coefficient (k) and refractive index (n). The experimental spectra of the investigated thin films are monotonic curves without oscillations. (Fig. 4).

Introduction of tin even in low concentrations leads to a change in both the real and imaginary parts of the complex refractive index. At the telecommunication wavelength (1.55 μm), the extinction coefficient monotonically increases up to several times, while the refractive index increases about by about 5% only, reaching its maximum at a value of 0.5 at.% Sn and then decreases. As a result, Sn doping can serve as a powerful tool to increase light absorption in nanophotonic devices, solving for specific tasks when necessary.

Thus, based on the results of the thin film investigation, the following improvements can be expected. Firstly, the formation of weaker Sn-Te bonds in GST225 thin films should lead to a decrease in the energy needed to switch the PCM film between the amorphous and crystalline states. Secondly, the increase of the extinction coefficient of GST225 films will lead to the growth of the effective absorption coefficient of the nanophotonic devices, which as a result, will be accompanied by the improvement of the conversion efficiency of the light pulse energy into heat. Next, we sequentially examined these hypothesizes, since noted effects play a decisive role in achieving a complex reduction in the energy consumption of the reconfigurable devices under development.

3.3. Investigation of the on-chip effective absorption coefficient

The influence of Sn doping on the effective absorption index of the nanophotonic devices based on GST225 thin films was examined by the experimental study of fabricated MZIs with different lengths of the PCM layer. The measured transmission spectra for the fabricated nanophotonic circuits with amorphous Sn-doped GST225 and undoped GST225 film coverings from 4 to 20 μm long are presented in Fig. 5. For clarity, each spectrum is shifted by 25 dB relatively to one another.

The measured spectra demonstrate periodic interference depending on the wavelength with free spectral range (FSR) ≈ 4 nm determined by the light path difference (ΔL = 280 μm) between the two arms of the MZI with waveguide effective refractive index (n_{eff}).

Fig. 5 is shown that tin doping leads to a change in the MZI transmission spectra depending on the PCM covering length and the level of Sn doping. Before GST225 thin film deposition, the MZI was balanced with the extinction ratio (ER) ≈ 20 dB. Deposition of the absorbing material leads to an imbalance of the MZI, which is due to the incomplete light interference at the output and also to the decrease of ER. The larger the absorbing area, the worse the balancing and the less the ER.

The output power P_{out} of MZI can be expressed by:

$$P_{out} = \frac{P_{in}}{4}\left(e^{-\mu l} + 1 + 2e^{-\mu l/2}\cos\left(2\pi n_{eff}\Delta L/\lambda\right)\right), \quad (1)$$

where P_{in} is the input power, μ is the attenuation coefficient and λ is wavelength of the light in vacuum.

In this case, ER, which is equal by definition to the ratio of the maximum (P_{max}) and minimum (P_{min}) transmitted powers, can be written as

$$\mathrm{ER} \equiv \frac{P_{max}}{P_{min}} = \frac{1 + 2e^{-\mu l/2} + e^{-\mu l}}{1 - 2e^{-\mu l/2} + e^{-\mu l}} = \frac{\left(1 + e^{-\mu l/2}\right)^2}{\left(1 - e^{-\mu l/2}\right)^2}, \quad (2)$$

while the attenuation coefficient μ can be extracted from Eq. (2):

$$\mu = -\frac{2}{l}\ln\left(\frac{\sqrt{\mathrm{ER}} - 1}{\sqrt{\mathrm{ER}} + 1}\right). \quad (3)$$

Fig. 6(a) shows the dependence of ER on the length of the amorphous PCM covering on the top of one of the MZI arms, calculated from the transmission spectra in Fig. 5(a) using Eq. (3).

Fig. 6(a) shows, on the one hand, that with an increase of the PCM covering length, the extinction ratio decreases, thereby confirming our initial qualitative statement about the imbalance of the interferometer. On the other hand, the Sn-doped GST225 has lower ER values compared to the undoped GST225. This indicates a higher attenuation coefficient value for the Sn-doped GST225.

It is possible to extract the attenuation coefficient using two ways. The first way is a numerical fit of ER(μ) according to Eq. (2) (green and black solid lines in Fig. 6(a), where μ is an unknown parameter. This way is fast, but not so visual. The second way requires obtaining the attenuation coefficient in a more explicit and visual form, substituting μ (Eq. (3)) in the Beer–Lambert law: $A[dB]=10 \times \log(e^{-\mu l})$. The calculated dependence of the attenuation on the PCM covering length is shown in Fig. 6(b), where the slope of the linear fit (green and black solid lines) shows the attenuation coefficient [dB/μm].

The attenuation coefficient includes light scattering (s), reflection (r) and absorption (α) coefficients in the general case. Numerical modeling performed by Rios et al. [74] showed that, due to evanescent mode coupling, the GST225 cell reflection is about −30 dB, therefore, the coefficient r can be neglected. Moreover, according to the calculated data, light scattering is significant for the PCM covering length up to 1–2 μm. The higher scattering losses take place in this case due to the PCM covering length which is on the same scale as the wavelength of light in the waveguide. In this work, we use a PCM covering length in the range of l = 4–20 μm, where absorption contributes mostly to the attenuation coefficient ($\mu \approx \alpha$). For this reason, the attenuation coefficient found here can be considered as effective absorption coefficient α.

The extracted values of α for the amorphous and crystalline thin films with each Sn concentration are shown in Fig. 6(c). It

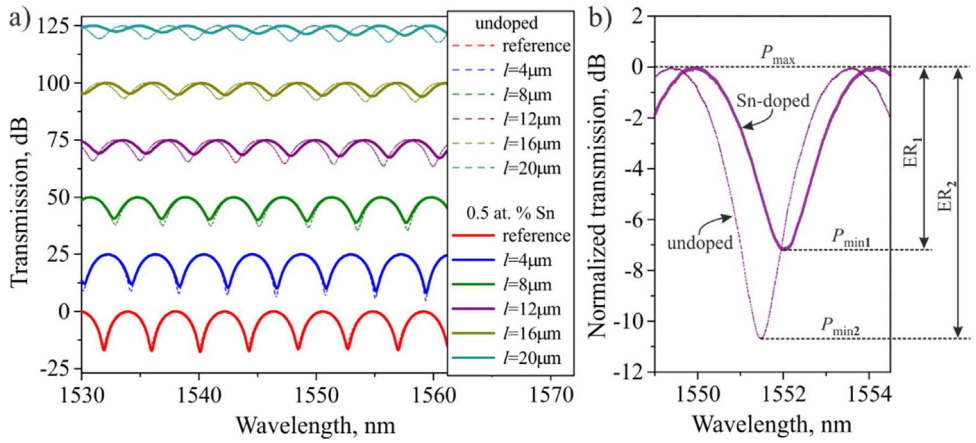

Fig. 5. (a) Measured transmission spectra for MZI devices with amorphous GST225 (dashed thin line) and amorphous Sn doped GST225 (solid thick line) for different values of the PCM covering length. Red solid and dashed lines show the reference devices without PCM thin film atop. For clarity, each spectrum is shifted by 25 dB relatively to one another. (b) Higher resolution spectrum of two resonance peaks shown in (a) (PCM covering length = 12 μm), demonstrating the difference in the extinction ratio between Sn-doped GST225 (0.5 at.% Sn) and undoped GST225 films. P_{max} and P_{min} are maximum and minimum powers, respectively.

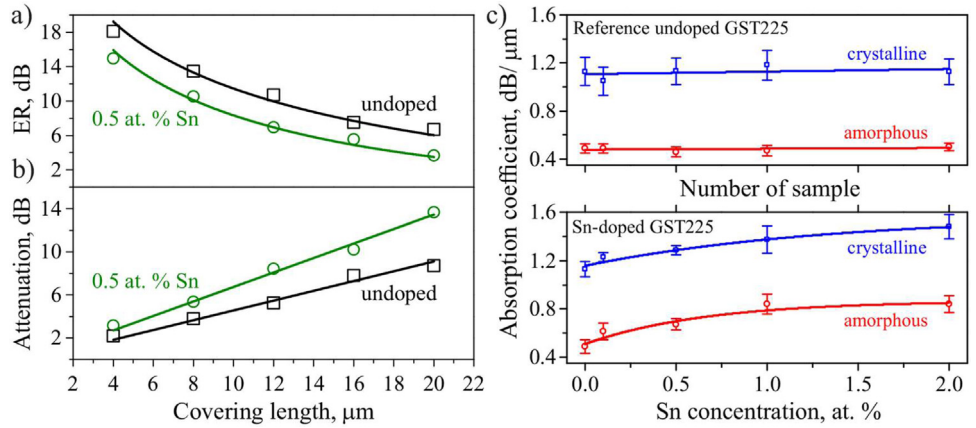

Fig. 6. (a) Dependence of the ER on the amorphous PCM covering length. The dots are the experimental data, and the lines correspond to the results of fitting using Eq. (2). (b) Dependence of the attenuation on the amorphous PCM covering length. The symbols are the experimental data, the lines correspond to the results of fitting using Eq. (3). (c) The dependence of the absorption coefficient for the amorphous and crystalline samples on the Sn concentration (bottom). The dependence of absorption coefficients for the reference structures of GST 225 (up). The undoped devices were made in the same cycle as the Sn-dopes ones, but they were covered with a metal mask during tin ions implantation. The graph shows that the metal mask protects the films well, and there is no change in the absorption coefficient.

should be noted, that amorphous and crystalline fractions coexist with each other after the optical switching of waveguide devices and the ratio between fractions depends on the pulse energy, geometric parameters of the PCM cell, the amorphous/crystalline distribution before an incoming pulse and the optical constants of PCMs [74]. So, we investigated the absorption coefficient of the devices with fully amorphous and crystalline PCM thin films, as two limiting cases. The study of such cases allows determining the maximum available difference between levels of logical 1 and 0 and carrying out their correct comparison. The samples were crystallized by annealing at 200 °C for 15 min in argon. The choice of the annealing temperature was based on the results of X-ray diffraction [61,68], according to which this temperature should allow crystallization of Sn-doped thin films into the same NaCl-type structure as GST225.

All amorphous undoped GST225, covered with a metal mask to protect doping during implantation (reference devices), show approximately the same effective absorption coefficient (0.48 ± 0.02 dB/μm). The crystallization of the reference undoped GST225 leads to an increase in the absorption coefficient to 1.12 ± 0.06 dB/μm. At the same time, Sn-doped samples show a steady tendency of the effective absorption coefficient increasing with the Sn concentration growing up for both phase states (see Fig. 6(c)). Since the values of this coefficient for the Sn-doped GST225 are obtained for the first time, it is possible to compare data only for the waveguides combined with the GST225 thin film. The extracted effective absorption coefficient for the amorphous and crystalline GST225 thin films is in agreement with the values obtained in [75,77].

The difference between amorphous and crystalline states of PCM thin films is a critically important parameter for the operation of optical devices, and, ideally, it determines the number of levels that can be reliably recorded and read. The results show that tin introduction leads to absorption changes not only in the amorphous, but also in the crystalline state. The optical difference between the two phase states, before and after doping the GST225 thin films, hardly changes. This difference in the effective absorption coefficient ranges from 0.61 to 0.64 dB/μm for the most investigated samples. An exception is the sample with 0.1 at.% Sn which demonstrated 0.55 dB/μm (its error bar in Fig. 6(c) is 0.06 dB/μm). This allows to conclude that the logical levels in the doped GST225 films can be recorded with a difference in absorption no worse than in the devices based on pure GST225.

The increase in effective absorption coefficient for the amorphous and crystalline states is definitely a good result from the point of view of lowering the switching energy since it will al-

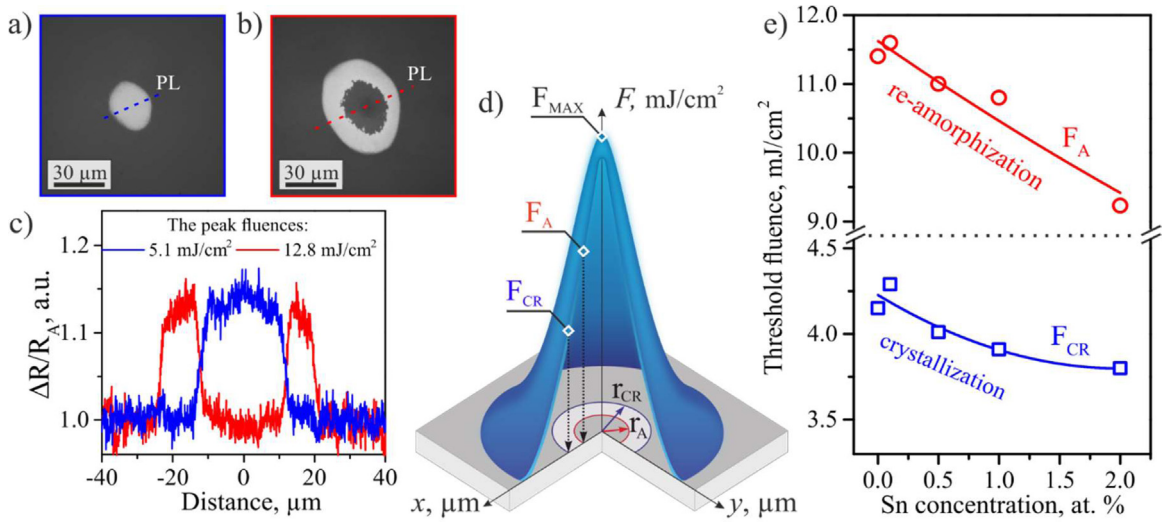

Fig. 7. (a, b) The magnified images of the laser crystallized and the amorphized marks formed on the GST225 with 2 at.% thin films after the irradiation with 500 number of pulses at F_{max} of 5.1 and 12.8 mJ/cm^2, respectively. (c) The profiles of $\Delta R/R_A$ along the profile line (PL). (d) The schematic diagram of the femtosecond laser energy distribution and the estimation of the crystallization and amorphization threshold fluences. (e) The effect of Sn ion implantation in GST225 thin films on the threshold fluences of the laser crystallization and amorphization.

low to improve the efficiency of conversion of the light pulse energy into heat. On the other hand, it should be noted that an increase in the absorption could also lead to negative consequences, in particular, to an increase in optical losses. This factor is an inevitable compromise for lowering power consumption with such an approach.

3.4. Investigation of the switching process

The undoped and implanted thin film samples were irradiated by the normally incident fs-laser beam with Gaussian profile for estimation of the influence of Sn doping on the laser energies necessary for switching the GST225 thin films between amorphous and crystalline states. The scheme of experimental setup is shown in Supplementary information, Fig. S3. The laser fluence ranged from 0.7 to 10.0 mJ/cm^2. It was estimated by averaging the total energy of the incident beam over the irradiated area using borders determined by a 1/e^2 intensity drop from the peak value.

Two types of spots after the laser irradiation were obtained for all the investigated thin films: solid marks, and marks having a shape of a toroidal shell ("ring-shaped roll"). Fig. 7(a), (b) shows the reflection optical micrographs of the solid and toroidal marks formed on the amorphous GST225 thin films with 2 at.% Sn upon the irradiation of pulses with the peak fluences (F_{max}) of 5.1 and 12.8 mJ/cm^2, respectively.

The profiles of $\Delta R/R_A$ along the spot diameters (Fig. 7c) were extracted from the presented optical micrographs. The values of ΔR were defined as R - R_A, where R is the reflectivity of investigated area, and R_A is the reflectivity of the as-deposited amorphous thin film. The solid marks and the annular region of the toroidal marks have similar reflectivity, higher than as-deposited amorphous thin films. The increase of the reflectivity is associated with the crystallization of the irradiated region, which is accompanied by a rise in the refractive index in the visible wavelength range compared with the amorphous thin film [91]. At the same time, the central region of the toroidal marks and the as-deposited amorphous thin films have close reflectivities. This can be explained by laser amorphization in the central region of the toroidal marks, where the intensity of the Gaussian laser beam is higher. The results of the Raman measurements confirm these phase transitions (Supplementary information, Fig. S5). Namely, the ratio of relative intensities for the two main peaks A and B on the Raman spectra has changed due to the crystallization, while the shapes of the Raman spectra for the laser-amorphized region and the initial amorphous one are close.

Since the pulse energy of our laser obeys the Gauss distribution and crystallized/amorphized regions have sufficiently clear borders, the threshold laser fluences of these phase transformations can be estimated (Fig. 7d). To extract these values from the two-dimensional local laser fluence distribution obtained by means of a CCD beam profiler, the following procedure was applied. First, the crystalline or amorphous areas (S_{th}) were determined from the optical images. Second, the value of the local laser fluence was found in such way that the values higher than the threshold fluence cover the same determined area S_{th} on the laser beam energy distribution image. The values of the threshold fluences, therefore, correspond to the edges of the crystalline/amorphous areas and could be considered as the threshold for these processes.

The effect of Sn ion implantation on the threshold fluences of the GST225 laser crystallization (F_{CR}) and amorphization (F_A) is presented in Fig. 7(e).

The values of F_{CR} and F_A are decreasing as the amount of Sn–Te bonds with lower binding energy than Ge–Te bonds increases. The increase in Sn-concentration up to 2 at.% leads to a decrease in F_{CR} from 4.2 to 3.8 mJ/cm^2 (9%) and in F_A from 11.4 to 9.2 mJ/cm^2 (19%) compared with the undoped GST225. Moreover, the results show that crystallization and amorphization processes in doped films can also be initiated by fs-laser irradiation, as in pure GST225.

As mentioned above, the reason for these phenomena can be both a decrease in the binding energy simplifying the structural rearrangement of the material and an increase of the absorption leading to the more efficient conversion of optical energy into thermal one. So, summarizing it can be noted, that incorporation of Sn-dopant into GST225 accompanied by the decrease of laser switching energy is clearly a positive effect, which can reduce the energy consumption of the reconfigurable nanophotonic circuits.

3.5. Multilevel reversible recording

The final stage of this work was demonstration of the possibility of using Sn-doped GST225 to provide reversible multilevel switching in the integrated nanophotonic devices. Such demonstration is very important since it proves the possibility of us-

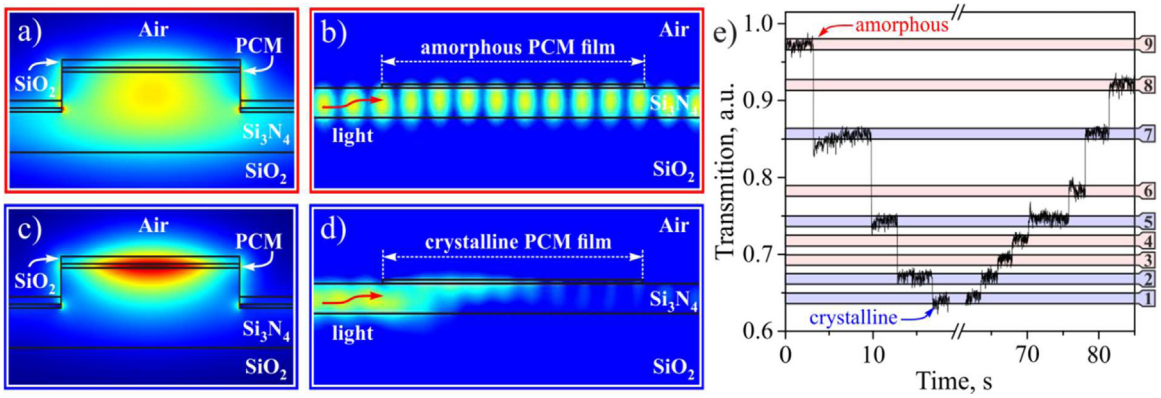

Fig. 8. Distribution of the electric field (quasi-TE mode) in a cross section of the silicon nitride waveguide coated (along and across the waveguide) with amorphous (a,b) and crystalline (c,d) PCM thin films with a covering layer of silicon dioxide. (e) Time dependence of a probe signal during 50 ns of the pump pulses absorption for the balance splitter on the basis of GST225 with 2 at.% Sn thin film.

ing Sn-doped GST225 layers to create the reconfigurable multilevel nanophotonic circuits.

As noted earlier, the operating principle of the fabricated devices is based on the significant changes in the optical properties of PCMs during phase transitions, accompanied by changes in waveguide's losses. Amorphous and crystalline states correspond to low and high optical losses, respectively. Fig. 8(a)–(d) shows the distribution of the electric field (quasi-TE mode) in cross sections of a silicon nitride waveguide coated with the amorphous and fully crystallized PCM thin films and a silicon dioxide cap, numerically calculated by COMSOL Multiphysics. The PCM covering length and waveguide width are 4 μm and 1 μm, respectively, which corresponds to one of the types of the fabricated samples. In the case of an amorphous PCM thin film, the waveguide mode remains in the center of the waveguide and attenuates slightly, whereas, for a fully crystallized film, the TE-mode is strongly rising to the top and is absorbed by PCM thin film. Thus, by controlling the ratio of crystalline and amorphous fractions, we can change the level of a light signal passing through a waveguide structure.

To confirm the possibility of using the Sn-doped GST225 thin films to implemented a reversible multilevel phase switching in integrated devices, we investigated switching in a fabricated balance splitter on a chip. The pump-probe experimental setup [see Experimental section and Supplementary Fig. S3] was used to form a single optical pump pulses for switching the Sn-doped GST225 cell of a nanophotonic device. The width of a single optical pump pulse was 50 ns and was limited by the speed of the optical amplifier.

By varying the pump pulse power, we were able to reversibly switch the devices based on all investigated Sn-doped GST225 thin films. The time dependence of the probe signal transmission demonstrating the multilevel switching between the logical states for a sample with 2 at.% Sn is shown in Fig. 8(e). The 9 nonvolatile different levels (3 bits) for the nanophotonic samples based on the Sn-doped GST225 thin films were demonstrated. The demonstrated number of logical levels is not a limit for the Sn-doped GST225 films and can be improved if the operational process strategy is optimized. Also, the optimized strategy will allow to set up the difference between states which greatly influences the reliability of the reversible multilevel phase switching in integrated devices.

It should be noted that switching between levels can be carried out both sequentially and through several levels (See Fig. 8e). The first option is suitable for creating a traditional memory cell. Unlike with flash memory, in such a cell the obligatory operation of erasing-before-recording-information will be eliminated. As for the second option, sequential recording is implemented without an abrupt change in properties, i.e. continuum of parameters. This option is required to create neuromorphic computations. The obtained results show that, with a switching strategy chosen wisely, our cells can operate in both modes.

4. Conclusion

The effect of tin ion implantation on the properties of amorphous GST225 thin films and influence of using such films on the parameters of silicon nitride nanophotonic circuits have been investigated. In the process of tin ion implantation Ge atoms were efficiently replaced by Sn due to the formation of low-energy Sn-Te bonds, which was accompanied by a change in the optical properties of the amorphous GST225 thin films. As a result, implantation led to the following results having positive complex effect on the energy consumption of laser switching processes.

First, it was shown that, the crystallization and amorphization processes in doped films can also be initiated by fs-laser irradiation, as in pure GST225. Wherein, as a result of the increase in weaker bond concentration and the extinction coefficient, the threshold laser energy of crystallization and amorphization processes, due to the pulse laser influence, noticeably decreased from 4.2 to 3.8 mJ/cm^2 (9%) and from 11.4 to 9.2 mJ/cm^2 (19%), respectively.

Secondly, for the first time, we have determined the effect of the tin dopant on the absorption coefficient of the crystalline and amorphous GST225 covers using the results of a direct study of waveguide structures. The results of the investigation of Mach-Zehnder interferometers showed that an increase in the concentration of Sn in GST225 leads to an increase in the effective absorption coefficient for the amorphous and crystalline GST225 covers in the on-chip devices. The optical difference between the two phase states, before and after doping the GST225 thin films, hardly changes. This difference in the effective absorption coefficient ranges from 0.61 to 0.64 dB/μm for the most investigated samples. This allows to conclude that the logical levels in the doped GST225 films can be recorded with a difference in absorption no worse than in the devices based on pure GST. On the one hand, this is definitely a positive result for lowering the laser switching energy, since it will improve the efficiency of converting the light pulse energy into heat. On the other hand, an increase in the effective absorption coefficient can also have negative effects. In particular, it can lead to bigger optical losses.

The possibility to use the Sn-doped GST225 thin films for fully optical multilevel reversible recording has been demonstrated by experimental measurements of fabricated on-chip balanced beam splitters. The reversible switching between 9 different levels (3 bits) both sequentially and through several levels without completely erasing the cell was performed. It should be noted that the

number of levels demonstrated is not a limit for Sn-doped GST225 films and can be improved if the operating process strategy is optimized.

Thus, the results of this work show that Sn-doping of the GST225 layer can be used to optimize the properties of the GST225 thin films, in particular to reduce the switching energy. So, it has the potential to improve the characteristics of reconfigurable multilevel nanophotonic devices using the GST225 thin films, including fully optical non-volatile memory and developed on-chip low power all-photonic circuits for post-von Neumann arithmetic processing. However, to estimate the future prospects of this approach, it is necessary to improve the device operation strategy, to determine the limiting number of switching cycles, and also to compare our approach with the other ones applied to improve the characteristics of electrical phase change memory devices, for example, Ge-rich GST225 and the heterostructures of alternating GeTe and Sb_2Te_3 monolayers.

Declaration of Competing Interest

The authors declare no conflict of interest

Acknowledgments

This work was supported by the Russian Science Foundation (project No. 20-79-10322; nanophotonic circuits design and fabrication). We also acknowledge the support by RFBR (project No. 20-07-01092, doped GST225 fabrication and study). The authors are grateful to Alexey Sitnikov and Dmitry Seleznev (National Research Center "Kurchatov Institute"-ITEP) for their assistance in performing our ion implantation into the films, Anna Dedkova (MIET) for ellipsometric measurements, Mikhail Smayev (Mendeleev University of Chemical Technology of Russia) for laser irradiation, and Yuliya Zaytseva (MIET) for TEM investigations of initial thin films. The studies of the irradiated thin film samples were performed using the equipment of the Core facilities centers “Diagnostics and modification of microstructures and nanoobjects”, "MEMS and electronic components", "STI Sensory" of MIET and “KAMIKS” center at NRC KI ITEP.

Supplementary materials

Supplementary material associated with this article can be found, in the online version, at doi:10.1016/j.actamat.2022.117994.

References

[1] C. Sun, M. Wade, Y. Lee, J. Orcutt, L. Alloatti, M. Georgas, A. Waterman, J. Shainline, R. Avizienis, S. Lin, B. Moss, R. Kumar, F. Pavanello, A. Atabaki, H. Cook, A. Ou, J. Leu, Y. Chen, K. Asanović, R. Ram, M. Popović, V. Stojanović, Single-chip microprocessor that communicates directly using light, Nature 528 (2015) 534–538, doi:10.1038/nature16454.

[2] A. Atabaki, S. Moazeni, F. Pavanello, H. Gevorgyan, J. Notaros, L. Alloatti, M. Wade, C. Sun, S. Kruger, H. Meng, K. Qubaisi, I. Wang, B. Zhang, A. Khilo, C. Baiocco, M. Popović, V. Stojanović, R. Ram, Integrating photonics with silicon nanoelectronics for the next generation of systems on a chip, Nature 556 (2018) 349–354, doi:10.1038/s41586-018-0028-z.

[3] N. Miyagawa, Overview of Blu-Ray DiscTM recordable/rewritable media technology, J. Front. Opt. 7 (2014) 409–424, doi:10.1007/s12200-014-0413-7.

[4] H. Cheng, F. Carta, W. Chien, H. Lung, M. BrightSky, 3D cross-point phase-change memory for storage-class memory, J. Phys. D: Appl. Phys. 52 (2019) 473002, doi:10.1088/1361-6463/ab39a0.

[5] Consulting Agency “Reports and data”. Phase Change Memory Market By Form (Standalone, and Embedded), By Technology, and By Applications, 2016-2026 (Industry report: https://www.reportsanddata.com/report-detail/phase-change-memory-market). 2019, p. 143.

[6] W. Dong, H. Liu, J. Behera, L. Lu, R. Ng, K. Sreekanth, X. Zhou, J. Yang, R. Simpson, Wide bandgap phase change material tuned visible photonics, Adv. Funct. Mater. 29 (2019) 1806181, doi:10.1002/adfm.201806181.

[7] Z. Guo, X. Yang, F. Shen, Q. Zhou, J. Gao, K. Guo, Active-tuning and polarization-independent absorber and sensor in the infrared region based on the phase change material of $Ge_2Sb_2Te_5$ (GST), Sci. Rep. 8 (2018) 12433, doi:10.1038/s41598-018-30550-2.

[8] Y. Qu, Q. Li, L. Cai, M. Pan, P. Ghosh, K. Du, M. Qiu, Thermal camouflage based on the phase-changing material GST, Light: Sci. Appl. 7 (2018) 1–10, doi:10.1038/s41377-018-0038-5.

[9] C. Hwang, G. Kim, J. Yang, C. Hwang, S. Cho, W. Lee, J. Pi, J. Choi, K. Choi, H. Kim, S. Lee, Y. Kim, Rewritable full-color computer-generated holograms based on color-selective diffractive optical components including phase-change materials, Nanoscale 10 (2018) 21648–21655, doi:10.1039/C8NR04471F.

[10] A. Redaelli, A. Pirovano, A. Benvenuti, A. Lacaita, Threshold switching and phase transition numerical models for phase change memory simulations, J. Appl. Phys. 103 (2008) 111101, doi:10.1063/1.2931951.

[11] X. Liu, X. Li, L. Zhang, Y. Cheng, Z. Yan, M. Xu, X. Han, S. Zhang, Z. Zhang, E. Ma, New structural picture of the $Ge_2Sb_2Te_5$ phase-change alloy, Phys. Rev. Lett. 106 (2011) 025501, doi:10.1103/PhysRevLett.106.025501.

[12] P. Guo, A. Sarangan, I. Agha, A review of germanium-antimony-telluride phase change materials for non-volatile memories and optical modulators, Appl. Sci. 9 (2019) 530, doi:10.3390/app9030530.

[13] M. Wuttig, H. Bhaskaran, T. Taubner, Phase-change materials for non-volatile photonic applications, Nat. Photonics. 11 (2017) 465–476, doi:10.1038/nphoton.2017.126.

[14] T. Matsunaga, N. Yamada, Y. Kubota, Structures of stable and metastable $Ge_2Sb_2Te_5$, an intermetallic compound in GeTe–Sb_2Te_3 pseudobinary systems, Acta Cryst. B 60 (2004) 685–691, doi:10.1107/S0108768104022906.

[15] A. Lotnyk, S. Bernütz, X. Sun, U. Ross, M. Ehrhardt, B. Rauschenbach, Real-space imaging of atomic arrangement and vacancy layers ordering in laser crystallised $Ge_2Sb_2Te_5$ phase change thin films, Acta Mater. 105 (2016) 1–8, doi:10.1016/j.actamat.2015.12.010.

[16] S. Kozyukhin, I. Nikolaev, P. Lazarenko, G. Valkovskiy, O. Konovalov, A. Kolobov, N. Grigoryeva, Direct observation of amorphous to crystalline phase transitions in Ge–Sb–Te thin films by grazing incidence X-ray diffraction method, J. Mat. Sci.: Mater. Electron. 31 (2020) 10196–10206, doi:10.1007/s10854-020-03565-7.

[17] K. Shportko, S. Kremers, M. Woda, D. Lencer, J. Robertson, M. Wuttig, Resonant bonding in crystalline phase-change materials, Nat. Mater. 7 (2008) 653–658, doi:10.1038/nmat2226.

[18] B. Kooi, M. Wuttig, Chalcogenides by design: functionality through metavalent, Adv. Mater. 32 (2020) 1908302, doi:10.1002/adma.201908302.

[19] B. Huang, J. Robertson, Bonding origin of optical contrast in phase-change memory materials, Phys. Rev. B 81 (2010) 081204, doi:10.1103/PhysRevB.81.081204.

[20] A. Kolobov, P. Fons, A. Frenkel, A. Ankudinov, J. Tominaga, T. Uruga, Understanding the phase-change mechanism of rewritable optical media, Nat. Mater. 3 (2004) 703–708, doi:10.1038/nmat1215.

[21] J. Raty, W. Zhang, J. Luckas, Ch. Chen, R. Mazzarello, Ch. Bichara, M. Wuttig, Aging mechanisms in amorphous phase-change materials, Nat. Commun. 6 (2015) 7467, doi:10.1038/ncomms8467.

[22] J. Raty, M. Wuttig, The interplay between Peierls distortions and metavalent bonding in IV–VI compounds: comparing GeTe with related monochalcogenides, J. Phys. D 50 (2020) 234002, doi:10.1088/1361-6463/ab7e66.

[23] C. Rí, M. Stegmaier, P. Hosseini, D. Wang, T. Scherer, C. Wright, H. Bhaskaran, W. Pernice, Integrated all-photonic non-volatile multi-level memory, Nat. Photonics. 9 (2015) 725–732, doi:10.1038/nphoton.2015.182.

[24] N. Youngblood, C. Ríos, E. Gemo, J. Feldmann, Z. Cheng, A. Baldycheva, W. Pernice, C. Wright, H. Bhaskaran, Tunable volatility of $Ge_2Sb_2Te_5$ in integrated photonics, Adv. Funct. Mater. 29 (2019) 1807571, doi:10.1002/adfm.201807571.

[25] J. Feldmann, N. Youngblood, C. Wright, H. Bhaskaran, W. Pernice, All-optical spiking neurosynaptic networks with self-learning capabilities, Nature 569 (2019) 208–214, doi:10.1038/s41586-019-1157-8.

[26] Z. Cheng, C. Ríos, N. Youngblood, C. Wright, W. Pernice, H. Bhaskaran, Device level photonic memories and logic applications using phase-change materials, Adv. Funct. Mater. 30 (2018) 1802435, doi:10.1002/adma.201802435.

[27] M. Rude, J. Pello, R. Simpson, J. Osmond, G. Roelkens, J. Tol, V. Pruneri, Optical switching at 1.55 µm in silicon racetrack resonators using phase change materials, Appl. Phys. Lett. 103 (2013) 141119, doi:10.1063/1.4824714.

[28] T. Moriyama, D. Tanaka, P. Jain, H. Kawashima, M. Kuwahara, X. Wang, H. Tsuda, Ultra-compact, self-holding asymmetric Mach-Zehnder interferometer switch using $Ge_2Sb_2Te_5$ phase-change material, IEICE Electr. Expr. 11 (2014) 20140538, doi:10.1587/elex.11.20140538.

[29] I. Chakraborty, G. Saha, A. Sengupta, K. Roy, Toward fast neural computing using all-photonic phase change spiking neurons, Sci. Rep. 8 (2018) 12980, doi:10.1038/s41598-018-31365-x.

[30] F. Rao, K. Ding, Y. Zhou, Y. Zheng, M. Xia, Sh. Lv, Zh. Song, S. Feng, I. Ronneberger, R. Mazzarello, W. Zhang, E. Ma, Reducing the stochasticity of crystal nucleation to enable subnanosecond memory writing, Science 358 (2017) 1423–1427, doi:10.1126/science.aao3212.

[31] M. Delaney, I. Zeimpekis, D. Lawson, D. Hewak, O. Muskens, A new family of ultralow loss reversible phase-change materials for photonic integrated circuits: Sb_2S_3 and Sb_2Se_3, Adv. Funct. Mater. 30 (2020) 2002447, doi:10.1002/adfm.202002447.

[32] K. Ding, J. Wang, Y. Zhou, H. Tian, L. Lu, R. Mazzarello, Ch. Jia, W. Zhang, F. Rao, E. Ma, Phase-change heterostructure enables ultralow noise and drift for memory operation, Science 366 (2019) 210–215, doi:10.1126/science.aay0291.

[33] M. Agati, F. Renaud, D. Benoit, A. Claverie, In-situ transmission electron microscopy studies of the crystallization of N-doped Ge-rich GeSbTe materials, MRS Commun. 8 (2018) 1145, doi:10.1557/mrc.2018.168.

[34] R. Golovchak, Y. Choi, S. Kozyukhin, Yu. Chigirinsky, A. Kovalskiy, P. Xiong-Skiba, J. Trimble, R. Pafchek, H. Jain, Oxygen incorporation into GST phase-

change memory matrix, Appl. Surf. Sci. 332 (2015) 533–541, doi:10.1016/j.apsusc.2015.01.203.
[35] G. Bourgeois, V. Meli, F. Mamun, F. Mazen, E. Nolot, E. Martinez, J. Barnes, N. Bernier, A. Jannaud, F. Laulagnet, B. Hemard, N. Castellani, M. Bernard, C. Sabbione, F. Milesi, T. Magis, C. Socquet-Clerc, M. Coig, J. Garrione, M. Cyrille, C. Charpin, G. Navarro, F. Andrieu, Carbon ion implantation as healing strategy for improved reliability in phase-change memory arrays, Micro. Rel. 11 (2021) 114221, doi:10.1016/j.microrel.2021.114221.
[36] J. Fu, X. Shen, Q. Nie, L.Wu G.Wang, Sh. Dai, T. Xu, R. Wang, Crystallization characteristics of Mg-doped $Ge_2Sb_2Te_5$ films for phase change memory applications, Appl. Surf. Sci. 264 (2013) 269–272, doi:10.1016/j.apsusc.2012.09.181.
[37] J. Seo, K. Song, H. Lee, Crystallization behavior of amorphous $Al_x(Ge_2Sb_2Te_5)_{1-x}$ thin films, Appl. Phys. 108 (2010) 064515, doi:10.1063/1.3471799.
[38] R. Roy, A. Louiset, M. Benoit, L. Calmels, Electronic structure and conductivity of off-stoichiometric and Si-doped $Ge_2Sb_2Te_5$ crystals from multiple-scattering theory, Phys. Rev. 99 (2019) 245124, doi:10.1103/PhysRevB.99.245124.
[39] S. Wei, H. Zhu, K. Chen, D. Xu, J. Li, F. Gan, X. Zhang, Y. Xia, G. Li, Phase change behavior in titanium-doped $Ge_2Sb_2Te_5$ films, Appl. Phys. Lett. 98 (2011) 231910, doi:10.1063/1.3597617.
[40] T. Zhang, B. Zhang, R. Shao, K. Zheng, Structural evolution and corresponding electrical properties of V-doped $Ge_2Sb_2Te_5$ with increased temperature, Mater. Lett. 128 (2014) 329–332, doi:10.1016/j.matlet.2014.04.181.
[41] Q. Wang, B. Liu, Y. Xia, Y. Zheng, R. Huo, Q. Zhang, S. Song, Y. Cheng, Zh. Song, S. Feng, Cr-doped $Ge_2Sb_2Te_5$ for ultra-long data retention phase change memory, Appl. Phys. Lett. 107 (2015) 222101, doi:10.1063/1.4936847.
[42] P. Guo, J. Burrow, G. Sevison, A. Sood, M. Asheghi, J. Hendrickson, K. Goodson, I. Agha, A. Sarangan, Improving the performance of $Ge_2Sb_2Te_5$ materials via nickel doping: towards RF-compatible phase-change devices, Appl. Phys. Lett. 113 (2018) 171903, doi:10.1063/1.5053713.
[43] K. Ding, K. Ren, F. Rao, Zh. Song, L. Wu, B. Liu, S. Feng, Study on the Cu-doped $Ge_2Sb_2Te_5$ for low-power phase change memory, Mater. Lett. 125 (2014) 143–146, doi:10.1016/j.matlet.2014.03.180.
[44] M. Choi, H. Choi, J. Ahn, Y. Kim, Material design for $Ge_2Sb_2Te_5$ phase-change material with thermal stability and lattice distortion, Scr. Mater. 170 (2019) 16–19, doi:10.1016/j.scriptamat.2019.05.024.
[45] V. Madhavan, M. Carignano, A. Kachmar, K. Sangunni, Crystallization properties of arsenic doped GST alloys, Sci. Rep. 9 (2019) 12985, doi:10.1038/s41598-019-49168-z.
[46] E. Vinod, K. Ramesh, K. Sangunni, Structural transition and enhanced phase transition properties of Se doped $Ge_2Sb_2Te_5$ alloys, Sci. Rep. 5 (2015) 8050, doi:10.1038/srep08050.
[47] Y. Huang, Y. Chen, T. Hsieh, Phase transition behaviors of Mo- and nitrogen-doped $Ge_2Sb_2Te_5$ thin films investigated by in situ electrical measurements, J. Appl. Phys. 106 (2009) 034916, doi:10.1063/1.3194787.
[48] P. Singh, P. Sharma, V. Sharma, A. Thakur, Linear and non-linear optical properties of Ag-doped $Ge_2Sb_2Te_5$ thin films estimated by single transmission spectra, Semicond. Sci. Technol. 32 (2017) 045015, doi:10.1088/1361-6641/aa5ee0.
[49] K. Wang, C. Steimer, D. Wamwangi, S. Ziegler, M. Wuttig, Effect of indium doping on $Ge_2Sb_2Te_5$ thin films for phase-change optical storage, Appl. Phys. A 80 (2005) 1611–1616, doi:10.1007/s00339-005-3232-2.
[50] Q. Yin, L. Chen, Enhanced optical properties of Sn-doped $Ge_2Sb_2Te_5$ thin film with structural evolution, J. Alloys Compd. 770 (2019) 692–700, doi:10.1016/j.jallcom.2018.08.169.
[51] S. Kumar, P. Sharma, V. Sharma, Dependence of structural cross-linking, system energy and transition temperature on coordination number for Sm doped GST, Results Phys. 13 (2019) 102276, doi:10.1016/j.rinp.2019.102276.
[52] R. Svoboda, V. Karabyn, J. Malek, M. Frumar, L. Benes, M. Vlcek, Amorphous-to-crystalline transition in $Ge_8Sb_{(2-x)}Bi_xTe_{11}$ phase-change materials for data recording, J. Alloys Compd. 674 (2016) 63–72, doi:10.1016/j.jallcom.2016.03.019.
[53] S. Guo, Z. Hu, X. Ji, T. Huang, X. Zhang, L. Wu, Z. Song, J. Chu, Temperature and concentration dependent crystallization behavior of $Ge_2Sb_2Te_5$ phase change films: tungsten doping effects, RSC Adv. 4 (2014) 57218–57222, doi:10.1039/c4ra08790a.
[54] R. Kojima, N. Yamada, Acceleration of crystallization speed by Sn addition to Ge–Sb–Te phase-change recording material, J. J. Appl. Phys. 40 (2001) 5930, doi:10.1143/JJAP.40.5930.
[55] K. Wang, C. Steimer, D. Wamwangi, S. Ziegler, M. Wuttig, J. Tomforde, W. Bensch, Influence of doping upon the phase change characteristics of $Ge_2Sb_2Te_5$, Microsyst. Technol. 13 (2007) 203–206, doi:10.1007/s00542-006-0156-5.
[56] W. Li, F. Liu, Y. Zhang, G. Han, W. Han, F. Liu, N. Sun, Crystallization accompanied by local distortion behavior of Sn-doped amorphous $Ge_2Sb_2Te_5$ induced by a picosecond pulsed laser, J. Non-Cryst. Solids 516 (2019) 99–105, doi:10.1016/j.jnoncrysol.2019.04.004.
[57] J. Dean, Lange's Handbook of Chemistry, McGRAW-HILL, USA, 2004.
[58] D. Kim, F. Merget, M. Laurenzis, P. Bolivar, H. Kurz, Electrical percolation characteristics of $Ge_2Sb_2Te_5$ and Sn doped $Ge_2Sb_2Te_5$ thin films during the amorphous to crystalline phase transition, J. Appl. Phys. 97 (2005) 083538, doi:10.1063/1.1875742.
[59] G. Singh, A. Kaura, M. Mukul, S. Tripathi, Electrical, optical, and thermal properties of Sn-doped phase change material $Ge_2Sb_2Te_5$, J. Mater. Sci. 48 (2013) 299–303, doi:10.1007/s10853-012-6745-z.
[60] T. Park, D. Kim, S. Yoon, K. Choi, N. Lee, B. Yu, S. Choi, Phase transition characteristics and device performance of Sn-doped $Ge_2Sb_2Te_5$ in phase change random access memory, J. J. Appl. Phys. 45 (2006) 1273–1276, doi:10.1143/JJAP.45.L1273.
[61] N. Bai, F. Liu, X. Han, Z. Zhu, X. Lin, N. Sun, A study on the crystallization behavior of Sn-doped amorphous $Ge_2Sb_2Te_5$ by ultraviolet laser radiation, Appl. Surf. Sci. 316 (2014) 202–206, doi:10.1016/j.apsusc.2014.08.007.
[62] S. Buller, Ch. Koch, W. Bensch, P. Zalden, R. Sittner, St. Kremers, M. Wuttig, U. Schürmann, L. Kienle, Th. Leichtwei, Ju. Janek, B. Schönborn, Influence of partial substitution of Te by Se and Ge by Sn on the properties of the blu-ray phase-change material $Ge_8Sb_2Te_{11}$, Chem. Mater. 24 (2012) 3582–3590, doi:10.1021/cm301809g.
[63] T. Park, S. Choi, M. Kang, Phase transition characteristics of Bi/Sn doped $Ge_2Sb_2Te_5$ thin film for PRAM application, Thin Solid Films 515 (2007) 5049, doi:10.1016/j.tsf.2006.10.045.
[64] M. Lee, K. Yong, Ch. Gan, L. Ting, S. Daud, L. Shi, Crystallization and thermal stability of Sn-doped $Ge_2Sb_2Te_5$ phase change material, J. Phys. D: Appl. Phys. 41 (2008) 215402, doi:10.1088/0022-3727/41/21/215402.
[65] S. Gu, L. Hou, Q. Zhao, R. Huang, Thermal phase change and activation energy of crystallization of Ge-Sb-Te-Sn thin films, Chin, Opt. Lett. 1 (2003) 716–718 https://www.osapublishing.org/col/abstract.cfm?URI=col-1-12-716.
[66] W. Song, L. Shi, X. Miao, T. Chong, Phase change behaviors of Sn-doped Ge–Sb–Te material, Appl. Phys. Lett. 90 (2007) 091904, doi:10.1063/1.2475390.
[67] M. Choi, H. Choi, J. Ahn, Y. Kim, Material design for $Ge_2Sb_2Te_5$ phase-change material with thermal stability and lattice distortion, Scr. Mater. 170 (2019) 16–19, doi:10.1016/j.scriptamat.2019.05.024.
[68] Q. Yin, L. Chen, Enhanced optical properties of Sn-doped $Ge_2Sb_2Te_5$ thin film with structural evolution, J. Alloys Compd. 770 (2019) 692–700, doi:10.1016/j.jallcom.2018.08.169.
[69] Ch. Xu, B. Liu, Zh. Song, S. Feng, B. Chen, Characteristics of Sn-Doped $Ge_2Sb_2Te_5$ films used for phase-change memory, Chin. Phys. Lett. 22 (2005) 2929–2932, doi:10.1088/0256-307x/22/11/056.
[70] X. Zhang, Zh. Zhang, S. Song, Q. Zheng, W. Yu, W. Zheng, X. Zhu, H. Shao, J. Zhang, L. Chen, Characterization of Ge ions implantation in Sb_2Te_3 thin films for high speed phase change memory application, Appl. Phys. Lett. 115 (2019) 103105, doi:10.1063/1.5109178.
[71] S.M. Serena Privitera. Ion Implantation in Phase Change Ge2Sb2Te5 Thin Films For Non Volatile Memory Applications. Italy, 2012. https://doi.org/10.5772/35338.
[72] D. Seleznev, A. Kozlov, T. Kulevoy, A. Sitnikov, P. Lazarenko, Y. Vorobyov, M. Smayev, A. Yakubov, A. Sherchenkov, S. Kozyukhin, The vacuum arc ion source for indium and tin ions implantation into phase change memory thin films, Rev. Sci Instrum. 90 (2019) 123313, doi:10.1063/1.5128561.
[73] S. Tripathi, P. Kotula, M. Singh, C. Ghosh, G. Bakan, H. Silva, C. Carter, Role of oxygen on chemical segregation in uncapped $Ge_2Sb_2Te_5$ thin films on silicon nitride, CS J. Solid State Sci. Technol. 9 (2020) 054007, doi:10.1149/2162-8777/ab9a19.
[74] C. Rios, M. Stegmaier, Z. Cheng, N. Youngblood, C. Wright, W. Pernice, Controlled switching of phase-change materials by evanescent-field coupling in integrated photonics, Opt. Mater. Express. 8 (2018) 2455–2470, doi:10.1364/OME.8.002455.
[75] J. Feldmann, N. Youngblood, X. Li, C. Wright, H. Bhaskaran, W. Pernice, Integrated 256 cell photonic phase-change memory with 512-bit capacity, IEEE J. Sel. Top. Quantum Electron. 26 (2020) 1–7, doi:10.1109/JSTQE.2019.2956871.
[76] C. Rios, P. Hosseini, C. Wright, H. Bhaskaran, On-chip photonic memory elements employing phase-change materials, Adv. Mater. 26 (2014) 1372–1377, doi:10.1002/adma.201304476.
[77] P. Nemec, V. Nazabal, A. Moreac, J. Gutwirth, L. Beneš, M. Frumar, Amorphous and crystallized Ge–Sb–Te thin films deposited by pulsed laser: local structure using Raman scattering spectroscopy, Mater. Chem. Phys. 136 (2012) 935–941, doi:10.1016/j.matchemphys.2012.08.024.
[78] Z. Xu, C. Chen, Z. Wang, K. Wu, H. Chong, H. Ye, Optical constants acquisition and phase change properties of $Ge_2Sb_2Te_5$ thin films based on spectroscopy, RSC Adv. 8 (2018) 21040–21046, doi:10.1039/C8RA01382A.
[79] T. Li, L. Wu, X. Ji, Y. Zheng, G. Liu, Zh. Song, J. Shi, M. Zhu, S. Song, S. Feng, Carbon doping induced Ge local structure change in as-deposited $Ge_2Sb_2Te_5$ film by EXAFS and Raman spectrum, AIP Adv. 8 (2018) 025201, doi:10.1063/1.5020614.
[80] M. Bouška, S. Pechev, Q. Simon, V. Nazabal, J. Gutwirth, E. Baudet, P. Nemec, Pulsed laser deposited GeTe-rich GeTe-Sb_2Te_3 thin films, Sci. Rep. 6 (2016) 26552, doi:10.1038/srep26552.
[81] R. Mazzarello, S. Caravati, S. Angioletti-Uberti, M. Bernasconi, M. Parrinello, Signature of tetrahedral ge in the raman spectrum of amorphous phase-change materials, Phys. Rev. Lett. 104 (2010) 085503, doi:10.1103/PhysRevLett.104.085503.
[82] F. Yang, L. Xu, J. Chen, J. Xu, Y. Yu, Z. Ma, K. Chen, Nanoscale multilevel switching in $Ge_2Sb_2Te_5$ thin film with conductive atomic force microscopy, Nanotechnology 27 (2015) 035706, doi:10.1088/0957-4484/27/3/035706.
[83] T. Gu, J. Wang, H. Liu, Z. Wang, Y. Luo, P. Liu, J. Zhong, G. Wang, One-step phase transition and thermal stability improvement of $Ge_2Sb_2Te_5$ films by erbium-doping, Vacuum 145 (2017) 258–261, doi:10.1016/j.vacuum.2017.09.008.
[84] J. Xu, Ch. Qi, L. Chen, L. Zheng, Q. Xie, The microstructural changes of $Ge_2Sb_2Te_5$ thin film during crystallization process, AIP Adv. 8 (2018) 055006, doi:10.1063/1.5025204.
[85] S. Kozyukhin, M. Veres, N. Nguen, A. Ingram, V. Kudoyarova, Structural changes in doped $Ge_2Sb_2Te_5$ thin films studied by Raman spectroscopy, Phys. Proc. 44 (2013) 82–90, doi:10.1016/j.phpro.2013.04.011.
[86] G. Sosso, S. Caravati, R. Mazzarello, M. Bernasconi, Raman spectra of cubic and amorphous GeSbTe from first principles, Phys. Rev. B 83 (2011) 134201, doi:10.1103/PhysRevB.83.134201.

[87] S. Sahu, Sh.K. Pandey, A. Manivannan, U.P. Deshpande, V.G. Sathe, V.R. Reddy, M. Sevi, Direct evidence for phase transition in thin $Ge_1Sb_4Te_7$ films using in situ UV–Vis–NIR spectroscopy and Raman scattering studies, Phys. Stat. Sol. B 253 (2016) 1069–1075, doi:10.1002/pssb.201552803.
[88] N. Matsuo, N. Kawamoto, H. Hamada, Internal stress in polycrystalline Si film recrystallized by excimer laser annealing, Jpn. J. Appl. Phys. 43 (2004) 532, doi:10.1143/JJAP.43.532.
[89] K. Andrikopoulos, S. Yannopoulos, A. Kolobov, P. Fons, J. Tominaga, Raman scattering study of GeTe and $Ge_2Sb_2Te_5$ phase-change materials, J. Phys. Chem. Solids 68 (2007) 1074–1078, doi:10.1016/j.jpcs.2007.02.027.
[90] J. Han, K. Jeong, M. Ahn, D. Lim, W. Yang, S. Park, M. Cho, Modulation of phase change characteristics in Ag-incorporated $Ge_2Sb_2Te_5$ owing to changes in structural distortion and bond strength, J. Mater. Chem. C 5 (2017) 3973–3982, doi:10.1039/C6TC05412A.
[91] Q. Yin, L. Chen, Enhanced optical properties of Sn-doped $Ge_2Sb_2Te_5$ thin film with structural evolution, J. Alloys Compd. 770 (2019) 692–700, doi:10.1016/j.jallcom.2018.08.169.